GEOPHYSICS, VOL. 74, NO. 2 (MARCH-APRIL 2009); P. F21–F29, 13 FIGS.
10.1190/1.3059600

# The feasibility of reservoir monitoring using time-lapse marine CSEM

Arnold Orange[1], Kerry Key[1], and Steven Constable[1]

## ABSTRACT

Monitoring changes in hydrocarbon reservoir geometry and pore-fluid properties that occur during production is a critical part of estimating extraction efficiency and quantifying remaining reserves. We examine the applicability of the marine controlled-source electromagnetic (CSEM) method to the reservoir-monitoring problem by analyzing representative 2D models. These studies show that CSEM responses exhibit small but measureable changes that are characteristic of reservoir-depletion geometry, with lateral flooding producing a concave-up depletion-anomaly curve and bottom flooding producing a concave-down depletion-anomaly curve. Lateral flooding is also revealed by the spatial-temporal variation of the CSEM anomaly, where the edge of the response anomaly closely tracks the retreating edge of the flooding reservoir. Measureable changes in CSEM responses are observed when 10% of the resistive reservoir is replaced by conductive pore fluids. However, to avoid corrupting the relatively small signal changes associated with depletion, the acquisition geometry must be maintained to a fraction of a percent accuracy. Additional factors, such as unknown nearby seafloor inhomogeneities and variable seawater conductivity, can mask depletion anomalies if not accounted for during repeat monitoring measurements. Although addressing these factors may be challenging using current exploration CSEM practices, straightforward solutions such as permanent monuments for seafloor receivers and transmitters are available and suggest the method could be utilized with present-day technology.

## INTRODUCTION

The utility of the marine controlled-source electromagnetic (CSEM) method for identifying hydrocarbon reservoirs was first demonstrated several years ago in a test by Statoil over the Girassol prospect, offshore Angola (Ellingsrud et al., 2002). Since then, the concept has been embraced with enthusiasm by the exploration industry, mainly as a tool for assessing the resistivity of targets identified by seismic surveys prior to drilling (e.g., Constable and Srnka, 2007). To a lesser extent, it has been used for estimating the size and extent of reservoirs, for estimating reservoir properties (Hoversten et al., 2006), and as a reconnaissance tool (Wahrmund et al., 2006). The logical next step is to apply the methodology to the production environment as a means of monitoring the geometry and porosity of reservoirs as they are depleted. This paper presents a simple feasibility study of the time-lapse or 4D CSEM approach as a prelude to conducting a field study.

The objective of reservoir-depletion monitoring is to determine the efficacy of the extraction and enhanced oil recovery (EOR) processes. The current approach to geophysical monitoring of reservoir depletion is to use time-lapse 3D seismic technology (e.g., Landro et al., 2003; Vasco et al., 2008), an approach that is in the early stages of development. If the feasibility of applying CSEM to this application is demonstrated, we anticipate that CSEM will prove to be highly complementary to time-lapse seismic data, as is the case with exploration CSEM (e.g., Darnet et al., 2007). The integration of CSEM data with other geophysical data sets, particularly high-quality 3D seismic data, is not considered in this paper, although this will be a critical part of any integrated geophysical approach to practical reservoir monitoring.

Previous studies implied the feasibility of CSEM for reservoir monitoring by showing that CSEM responses are sensitive to the lateral extent and thickness of resistive bodies (Constable and Weiss, 2006). Of particular interest is the sensitivity of CSEM to the edges of a resistive body embedded in a more conductive surrounding medium, which is directly relevant to offshore reservoir monitoring. Our objective is to examine the changes in the magnitude of CSEM responses as the reservoir edges are moved, simulating a retreating boundary where conductive pore fluids replace resistive hydrocarbons during reservoir production. Lien and Mannseth (2008) consider this problem using 3D integral-equation modeling and find that indeed the time-lapse CSEM signal exhibits measureable changes in response to reservoir production. We expand on their work by using

Manuscript received by the Editor 12 May 2008; revised manuscript received 3 October 2008; published online 3 March 2009.
[1]University of California San Diego, Scripps Institution of Oceanography, La Jolla, California, U.S.A. E-mail: aorange1@compuserve.com; kkey@ucsd.edu; sconstable@ucsd.edu.

accurate 2D finite-element modeling to study several variations of a depleting reservoir, including lateral and bottom flooding, stacked reservoirs, and partial-depletion effects. Because the total volume of oil or gas extracted from a reservoir is a known quantity, CSEM must be able to discriminate between such different depletion scenarios to be useful. Additionally, we present several acquisition and environmental factors that could confound time-lapse interpretations.

Reservoir-depletion monitoring is the primary force driving this research, but there are other possible applications for offshore time-lapse CSEM monitoring, such as $CO_2$ sequestration, waste sites, freshwater aquifers, seafloor volcanoes, hydrothermal vents, and geothermal regions, which may exhibit time-varying conductivity structure. Our studies also demonstrate the sensitivity of exploration CSEM to the size and shape of 2D reservoirs.

Our paper is organized as follows: In the first section, we present the modeling methodology and show how the CSEM responses for 2D depletion scenarios are characteristic of the flooding geometry. We then study a few environmental and acquisition factors that could confound the CSEM interpretation if not properly accounted for. We conclude the paper with a discussion of practical considerations for offshore CSEM monitoring and provide suggestions for data acquisition protocols that can address the high levels of accuracy and repeatability required.

## 2D RESERVOIR-DEPLETION STUDIES

In this section we present a 2D analysis of simplified models of reservoir depletion. Previous studies consider the sensitivity to thin

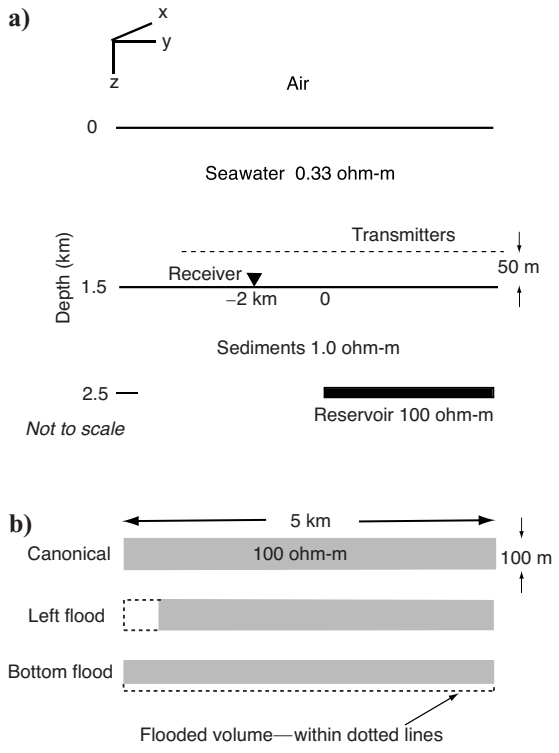


Figure 1. (a) The 2D canonical model used for the simulations. The single receiver is located at position −2 km, and the transmitters are positioned 50 m above the seafloor and are spaced at 250-m intervals from −4 to 15 km. The transmissions are computed at 0.1 Hz. (b) The reservoir geometry for the canonical, left, and bottom flooding models.

1D resistive structures and show that the inline CSEM response varies almost linearly with reservoir thickness (e.g., Figure 10 in Constable and Weiss, 2006). Although 1D studies are useful for generating basic CSEM insights, they are not applicable to monitoring problems because the finite width of the reservoir is a critical parameter in quantifying the nature of extraction.

More importantly, the 2D results we present for the model in Figure 1 demonstrate that the lateral edges of the reservoir impart a strong signal in the CSEM responses (Figure 2). Later, we show that this signal varies substantially as the reservoir is depleted. The 2D model responses in Figure 2 are qualitatively similar to the responses for a 3D resistive disk shown in Constable and Weiss (2006), and both 2D and 3D responses are significantly different from the 1D response past the edges of the resistive body. Actual survey data may require 3D tools, but we propose that 2D studies are a sufficient starting point for generating insights on the time-lapse monitoring problem.

We expect that low percentage-depletion scenarios will only generate small changes in the CSEM responses. To quantify these changes accurately, we need to consider the accuracy of our numerical modeling approach. Here, we use the MARE2DCSEM code (modeling with adaptively refined elements for 2D CSEM; Li and Key, 2007), which uses an adaptive finite-element method to generate arbitrarily accurate 2.5D CSEM responses. Although accurate responses can be generated by manually creating a very densely gridded finite-element mesh, MARE2DCSEM constructs a much more efficient mesh by automatically performing adaptive mesh refinement until the CSEM responses reach a user-specified accuracy.

The code accomplishes this by using a superconvergent gradient recovery operator to estimate the solution error in each element of the mesh. This error is then weighted by an adjoint solution of the

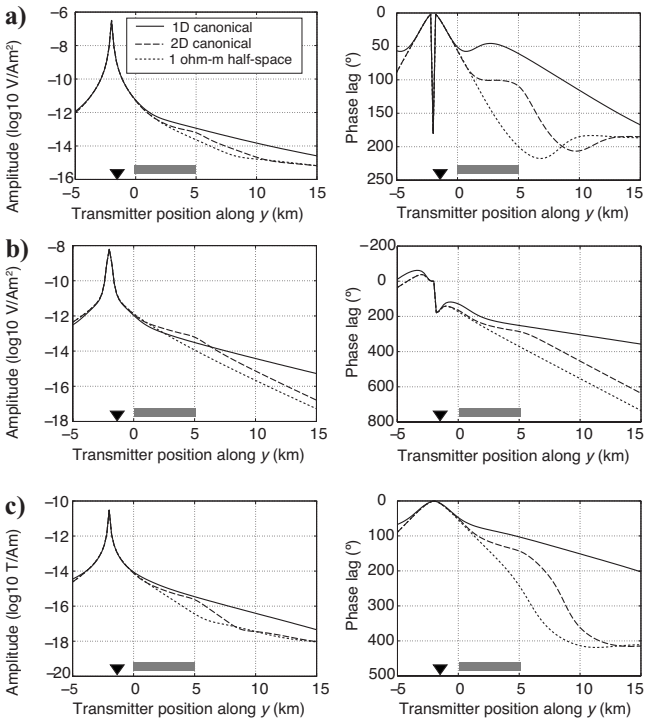


Figure 2. CSEM responses for the 1D and 2D canonical models and a 1-ohm-m half-space are shown for (a) the inline electric field $E_y$, (b) vertical electric field $E_z$, and (c) azimuthal magnetic field $B_x$.

2.5D differential equation, where the sourcing functions are the estimated errors at the discrete EM receivers. The adjoint solution provides an influence, or sensitivity, function for the global mesh errors. Thus, only elements with errors that contribute to the solution error at the discrete EM receivers are refined. Details of the adaptive refinement method and a validation of the method's accuracy for CSEM modeling are given in Li and Key (2007). For the model simulations presented here, we set the tolerance so that the finite-element mesh was refined until the estimated relative error in the CSEM responses was below 0.1%.

## Base model

The base model for our simulations is the 2D canonical model, shown in Figure 1a. This model is the 2D analog of the 1D canonical reservoir model presented in Constable and Weiss (2006) and consists of a 100-m-thick, 5-km-wide, 100-ohm-m reservoir buried 1000 m below the seafloor with an ocean depth of 1500 m. For the monitoring simulations, we perturb the model by depleting (flooding) the reservoir by raising the bottom surface (bottom flood, Figure 1b) or by moving the left edge inward (left flood, Figure 1b) over a range of depletions that vary from 0–80%. We model the CSEM responses for a single receiver located 2 km to the left of the reservoir for a series of inline electric dipole transmitters spaced every 250 m from −4 to 15 km horizontal position at 50 m above the seafloor. The transmitter and receiver computations assume a point dipole approximation, and all models are computed for 0.1-Hz transmissions.

Figure 2 shows the CSEM amplitude and phase responses for the 1D and 2D canonical models and a uniform half-space seafloor model. As mentioned, the 2D responses differ substantially from the 1D responses, and all field components show an inflection when the transmitter is over the right edge of the reservoir. Figure 2 identifies where the responses are larger than the noise floor of present-day transmitter-receiver systems (around $10^{-15}$ V/Am$^2$ for electric fields and $10^{-18}$ T/Am for magnetic fields). For instance, the inline electric field is above this noise floor where the transmitter is located at positions less than 12 km (i.e., up to 14 km source-receiver offset).

For the remainder of the model studies, we present the CSEM responses as the ratio of the responses for the model with the reservoir to that of the 1D half-space case, i.e., to the case without the reservoir. The plots are thus of the relative anomaly caused by the presence of the reservoir (canonical, or perturbed by flooding) in an otherwise uniform 1-ohm-m half-space. The phase of the CSEM responses clearly contains useful 2D structural information (see Figure 2), yet for brevity we restrict most of our analysis here to studying amplitude anomalies.

## Lateral and bottom flooding

In Figure 3, we present an anomaly comparison for models of bottom depletion with models of depletion laterally from the left. The cases shown are for no flood (2D canonical model) and for a flood (completely water-filled reservoir volume) of 10%, 20%, 40%, 60%, and 80%. The water-filled portion of the reservoir has the same resistivity as the background half-space (1 ohm-m). Currently, the most commonly collected data are the horizontal electric field, designated $E_y$ for radial-mode 2D modeling (Figure 3a). We also show the results for the vertical electric field $E_z$ (Figure 3b and the azimuthal magnetic field $B_x$ (Figure 3c). The results for each of the lateral-flood and bottom-flood comparisons are plotted to the same scale for each component.

Figure 3 shows that the reservoir-caused anomalies are strongest when the transmitter is over the far edge of the reservoir (near 5 km), and this peak anomaly resides at this position even in the presence of significant flooding. Thus, the distal edge of the reservoir seems to be an ideal transmission location (or, through Lorentz reciprocity, an ideal receiving location) for exploration and monitoring field surveys. There is little anomalous response when the transmitter is over the near edge (0 km) because of the absence of resistive structure between the source and receiver and the relatively shallow sensitivity at short offsets. For lateral and bottom flooding, the strongest anomaly is present in the azimuthal magnetic field; the weakest anomaly (still of considerable size) is in the inline electric field. For lateral flooding, the left edge of the anomalies moves in direct correspondence with the flooded edge of the reservoir, suggesting that CSEM monitoring may be able to distinguish which sides of the reservoir retreat during production.

Figure 4 shows the anomaly strength at 5 km as a function of flooding percentage. The anomaly magnitudes shrink as flooding increases, but the behavior of this decrease differs for the two flooding types. For all three components, flooding from the left results in a large decrease in anomaly amplitude during the early stages of depletion, which then slows down in the later stages, giving a concave-up depletion-anomaly curve. The opposite is seen for the basal

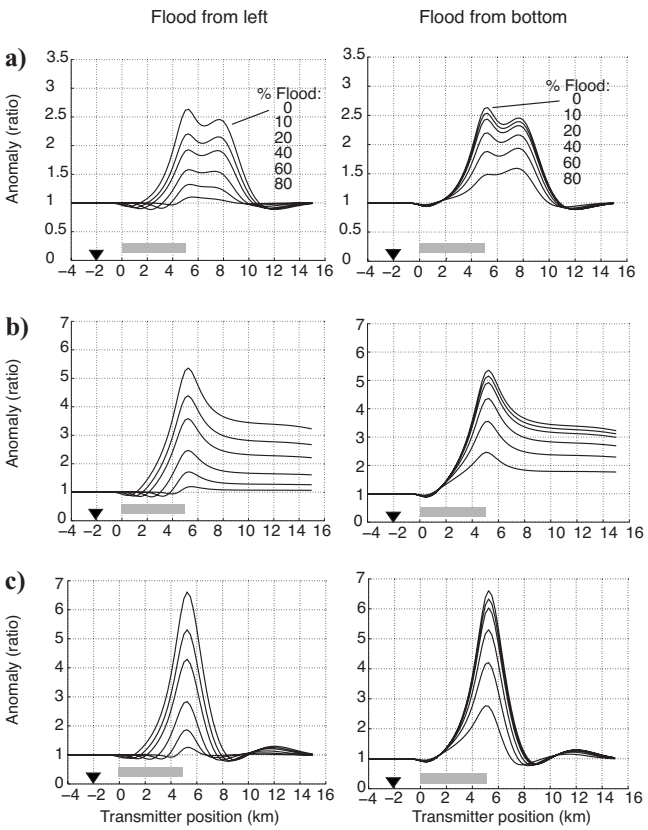


Figure 3. Depletion simulations for left flooding (left column) and bottom flooding (right column). The (a) inline electric field $E_y$, (b) vertical electric field $E_z$, and (c) azimuthal magnetic field $B_x$ amplitude anomalies are shown as the ratio of the 2D to half-space responses. Percent flood refers to the percent volume replaced by 1-ohm-m material, identical to the background resistivity.

flooding, where the early stages of flooding produce only small anomaly changes but late stages of flooding give a significant anomaly decrease, resulting in a concave-down depletion-anomaly curve. This systematic behavior may be a simple and useful tool for distinguishing between flooding types, although whether this holds for more complicated reservoirs remains to be studied. A corollary of the interpretation of Figure 3 that applies to exploration CSEM is that thin and wide reservoirs produce larger CSEM responses than thick and narrow reservoirs.

There are other subtleties associated with evaluating reservoir-depletion characteristics using CSEM. Consider the two sets of curves for the radial electric field $E_y$ in Figure 3a. The response for a 40% bottom flood is very similar to that for a 10% lateral flood. Likewise, the 80% bottom flood has an anomaly similar to the 40% lateral flood case. If the original reservoir volume is known, then the total production volume could be used to discriminate between left and bottom flooding models in these examples. The curve shapes for these reservoir geometries differ and provide a modicum of diagnostic evidence for determining where flooding occurs. The same observations could be made for the other field components.

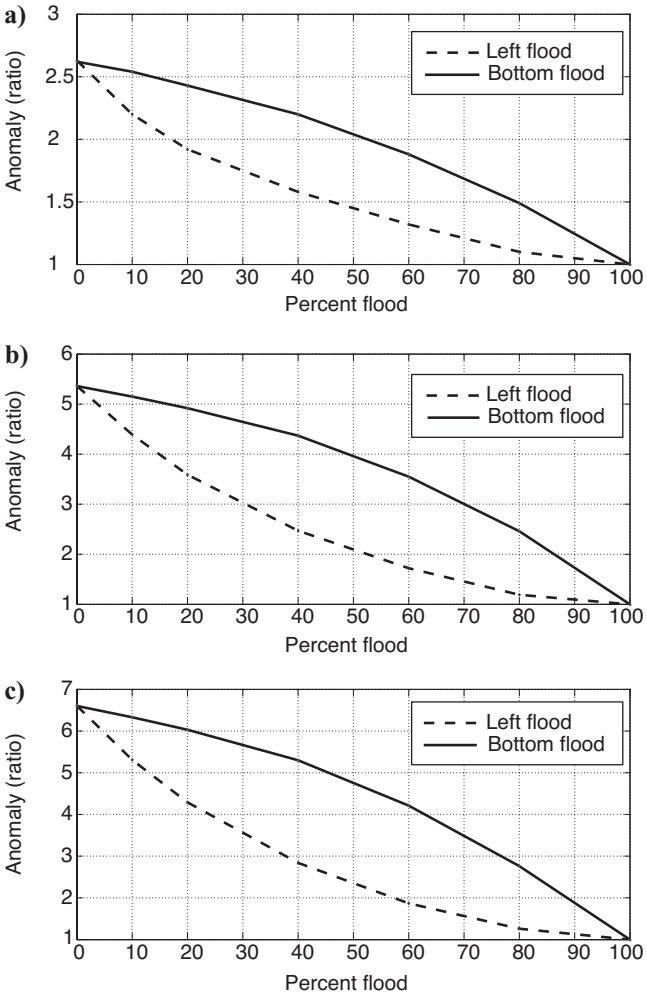


Figure 4. Anomaly strength as a function of percent depletion for when the transmitter is located over the right edge of the reservoir (5 km). The (a) inline electric field $E_y$, (b) vertical electric field $E_z$, and (c) azimuthal magnetic field $B_x$ are shown for left and bottom flooding.

## Effect of water depth

We also computed responses for the flooded reservoir models at a different water depth to study the effect of the airwave, a term used to describe energy that propagates along the air-sea interface. At short offsets, the fields measured by the receivers predominantly diffuse through the ocean and seabed; at longer offsets, the fields result from a combination of the airwave and diffusion through the reservoir and seabed (Constable and Weiss, 2006). The fields observed on the seafloor are the result of constructive or destructive interference between the airwave and reservoir wave, as determined by their respective amplitudes, phases, and vector orientations.

Because the airwave experiences complex attenuation as it diffuses from the transmitter up to the sea surface and later back down to the seafloor, the long-offset fields observed on the seafloor vary substantially with ocean depth. (See also Weidelt [2007] for a theoretical analysis of EM waves guided in the resistive air and reservoir layers.) In the example that follows, we demonstrate how the airwave's dependence on the ocean depth can affect the magnitude of CSEM anomalies significantly.

Figure 5 shows the anomaly responses for the lateral flooding case for ocean depths of 1500 and 3000 m and flooding of 0%, 10%, and 20%, with all other parameters as in Figure 3. The plots on Figure 5 use the same vertical scale for each component, emphasizing the large variations in the size of the reservoir-induced anomaly with ocean depth. This variation is inconsistent among the three field

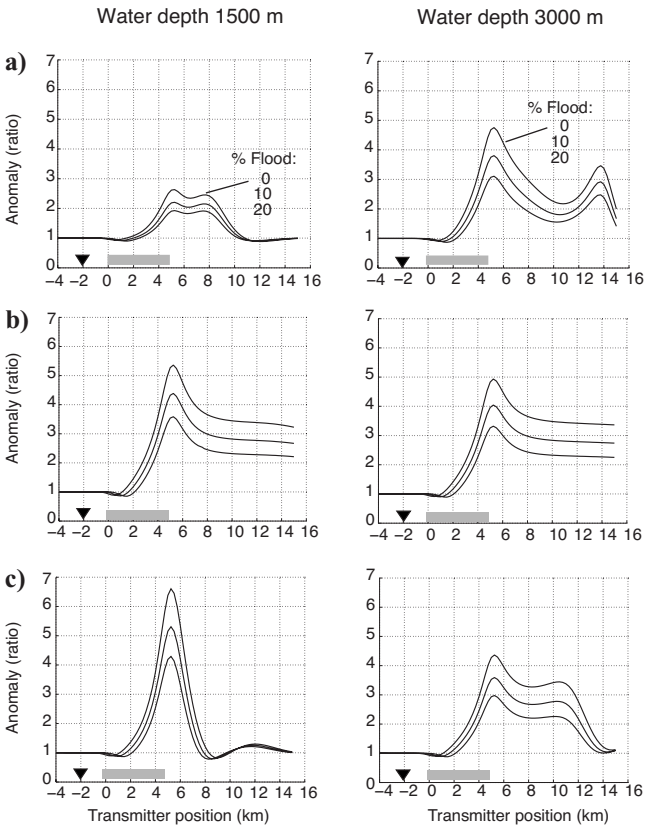


Figure 5. The effect of ocean depth on the anomaly amplitudes. (a) Inline electric field $E_y$, (b) vertical electric field $E_z$, and (c) azimuthal magnetic field $B_x$ anomalies associated with the perturbations of the 2D canonical model for two water depths: 1500 m (left column) and 3000 m (right column).

components. For $E_y$ (Figure 5a), the anomaly at 3000 m ocean depth is about double that at 1500 m; the reverse is true for $B_x$ (Figure 5c). Other changes appear at positions greater than 8 km, where $E_y$ for a 3000-m ocean depth has a second anomaly peak at about 14 km and $B_x$ has a second peak at about 11 km. Clearly, these second peaks are related to the ocean depth, showing that the airwave is strongly coupled to the sea layer (because the anomaly varies with ocean depth) and coupled with the wave traveling up from the reservoir (because an anomaly is present).

Although not shown here, systematic variation of the ocean depth from 1500 to 3000 m shows that these second anomaly peaks move to increasingly farther distances as water depth increases. We conclude that for a 1500-m ocean depth, the airwave-influenced response begins near the middle of the reservoir, but for a 3000-m ocean depth, the airwave does not affect the responses until a few kilometers past the edge of the reservoir.

The ability to detect the flood with the horizontal components appears not to be affected in either case because the relative changes between flood-induced anomalies is nearly constant in the vicinity of the reservoir. As anticipated, the vertical electric field ($E_z$, Figure 5b) is influenced least by the changes in the water depth.

## Stacked reservoirs

The canonical reservoir (Figure 1a) is clearly an oversimplification of most real-world reservoirs. Figure 6a depicts a somewhat more complex scenario: a three-layer reservoir sequence where the total vertical resistance (layer thickness times layer resistivity) of the three layers is equivalent to that of the single-layer canonical model. The three 20-m-thick, 166.6-ohm-m layers with 20-m-thick, 1-ohm-m intervals between the layers span the same 100-m total thickness of the canonical model. Although not shown here, the responses for this model differ from the canonical 2D model shown in Figure 1a by less than 0.5% for all three components — that is, this layered reservoir has nearly the same response as the 2D canonical reservoir. This unsurprising result suggests that CSEM will be limited in the ability to resolve closely spaced reservoir units, and to do so will require some significant a priori structural constraints.

We modeled a 20% depletion of the center of the three layers (Figure 6b) to evaluate the results of a more subtle depletion scenario. This corresponds to a 7% flood of the complete three-layer reservoir. Figure 7 shows the ratio of the CSEM response of the three-layer unflooded model to that of the model with a 20% flood of the center lay-

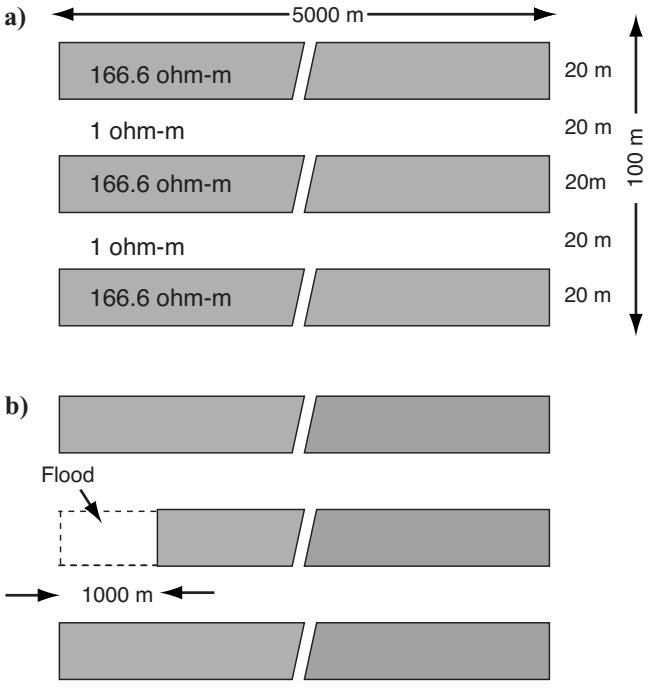


Figure 6. (a) Multilayer (anisotropic) reservoir model with a total vertical resistance of the combined three layers identical to the canonical model shown in Figure 1a. (b) A 20% flood of the middle layer of the model in (a).

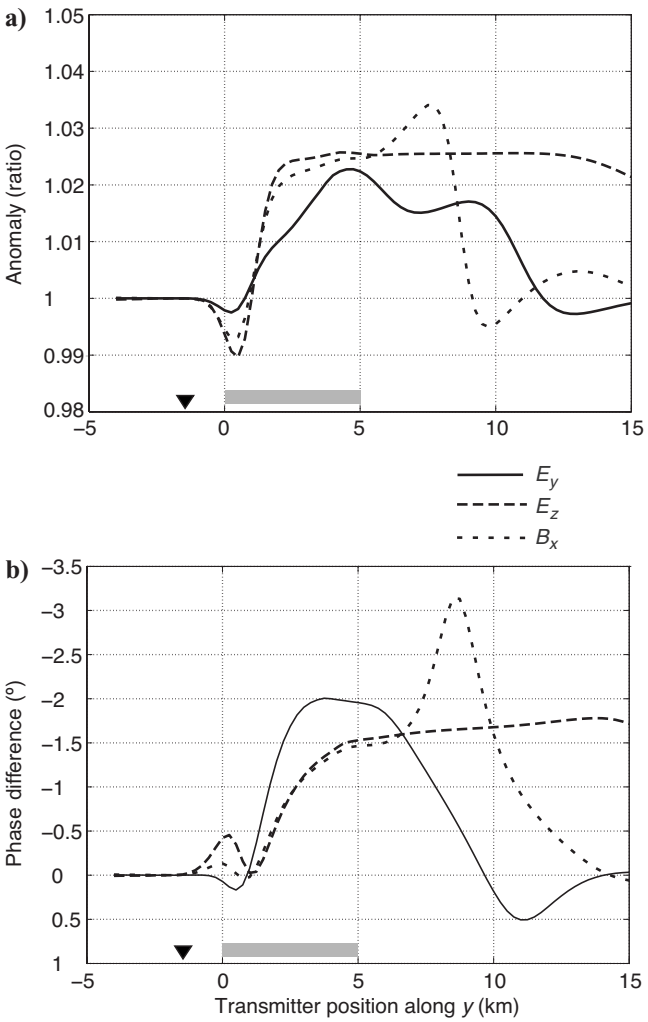


Figure 7. (a) Anomaly ratio and (b) phase difference for the three-layer reservoir model without flood (Figure 6a) compared to the three-layer model with 20% flood of the middle layer (Figure 6b).

er. The maximum anomaly is on the order of 2–4%, with the largest anomaly on the $B_x$ component. For each component, the anomaly onset occurs at or near the left edge of the reservoir assembly, coincident with flooding from the left.

## Partial-depletion effects

Given current extraction efficiencies, it is likely that a significant residue of hydrocarbons will remain in the flooded section of the reservoir, and it is important to consider the impact this may have on time-lapse CSEM. Consider the case where the production engineer states that 20% volume of the reservoir has been extracted. Figure 8 shows five variations of left flooding for this scenario, where the width of the flooded section depends on the fraction of hydrocarbons remaining in place. Model A is for complete extraction (100% depletion), as used for the previous studies shown here. Models B-E show a varying percentage of depletion in the flooded section (80–20%). The resistivity of the partially depleted section is computed as a function of the pore space occupied by water using Archie's law: $\rho = \rho_f(\phi d)^{-2}$, where the water resistivity $\rho_f = 0.16$ ohm-m, the porosity $\phi = 40\%$, and $d$ is the reservoir-depletion factor.

Figure 9 shows the CSEM anomalies for these scenarios. Model A (100% depletion) shows the largest anomaly; model D (40% depletion) shows the weakest anomaly. These end members' anomalies are about 10% different for the $E_y$ component and 30% different for the $E_z$ and $B_x$ components. Models A-D all have relatively low resistivity in the flooded section; hence, the anomalies correlate largely with the size of the unflooded reservoir section. Model E reverses the decreasing anomaly trend and exhibits a larger anomaly than model D. However, this is easily explained because model E has more remaining oil in place in the flooded section (i.e., the entire reservoir) and hence has a much higher resistivity than model D.

The difference in anomalies between any of these models is at least a few percent, suggesting that exploration or time-lapse CSEM could be used to discriminate between varying degrees of reservoir saturation. Furthermore, there is at least a 25% difference in anomaly size between any of these models and the 0% extraction (i.e., 0% flooded) models shown in the left column of Figure 3, indicating that all of these scenarios produce measureable time-lapse signals.

We have presented variations for only a few model parameters; clearly, this work could be expanded to study the effects of frequency, depth of reservoir burial, reservoir thickness, variable background resistivity, resistivity contrasts, and the multiple receiver locations typical of CSEM field surveys. However, the results presented here are representative based on many other 2D computations we have made.

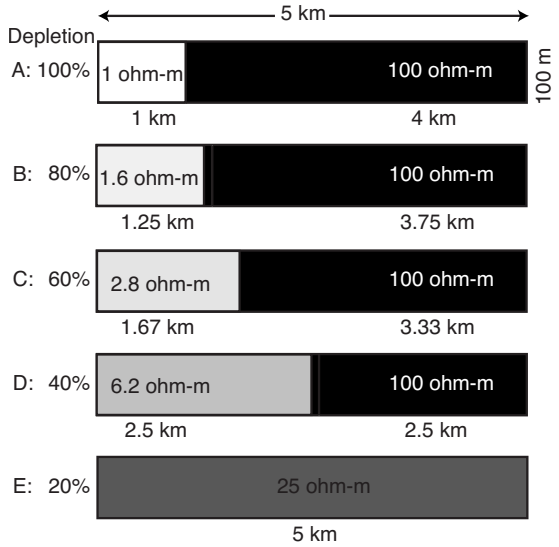


Figure 8. Five reservoir models representing 20% recovery of the original reservoir volume caused by flooding from the left. Models A–E show decreasing levels of depletion in the flooded region.

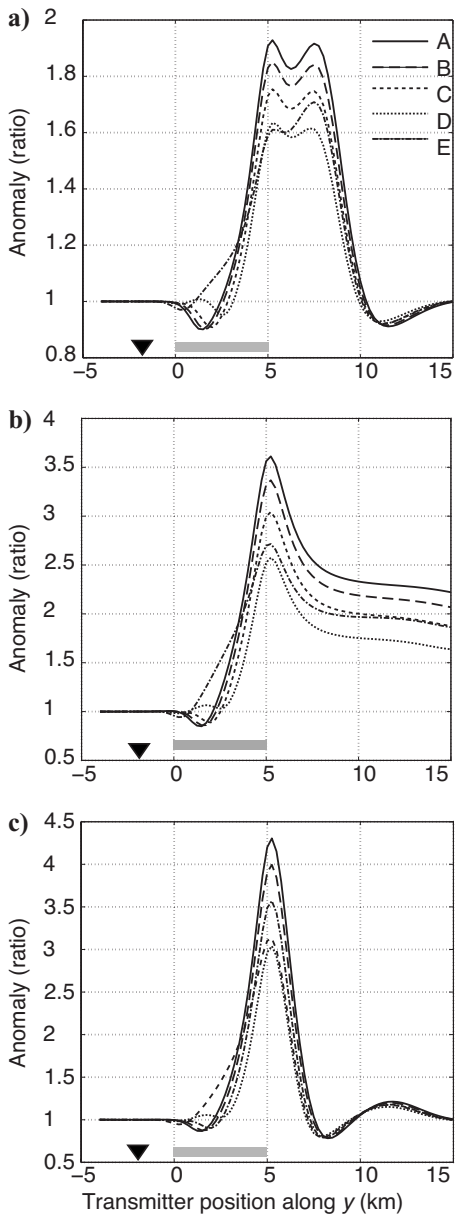


Figure 9. Anomaly ratios for the five partial-depletion models shown in Figure 8. Anomalies are computed by normalizing by a half-space response. The (a) inline electric field $E_y$, (b) vertical electric field $E_z$, and (c) azimuthal magnetic field $B_x$.

## FACTORS AFFECTING CSEM RELIABILITY

It is clear from the model studies that for time-lapse CSEM to succeed, measurement repeatability must be better than 5% — possibly better than 1–2% — to characterize the flooding geometry. Obviously, it will not be good enough to state that the reservoir is shrinking because the production manager knows that from the production rates. The subtle changes expected in reservoir geometry as the reservoir is depleted will require the ability to measure equally subtle changes in the CSEM response. In this section we present some examples of factors that could affect CSEM reliability — notably, the repeatability and accuracy required for time-lapse interpretation. These factors affect exploration use of CSEM as well for those cases where the expected anomalies are only slightly larger than the system noise floor and navigation uncertainties.

### Effect of near-surface inhomogeneities

The near-surface environment should not be expected to be homogeneous in every case. For example, Weitemeyer et al. (2006) use CSEM field data to constrain significant shallow resistivity variations associated with methane hydrates and free gas. Other studies consider how shallow structures can create significant CSEM anomalies (e.g., Darnet et al., 2007). Here, we present an example that demonstrates that a small near-surface resistive body can produce anomalies of size comparable to those of a depleting reservoir.

The model is shown in Figure 10a and includes the standard 2D canonical reservoir (Figure 1a) but with a 10-m-thick, 100-m-wide, 5-ohm-m body placed on the seafloor 2 km from the left edge of the reservoir. We computed the CSEM responses for a series of receivers placed on and adjacent to the body, as shown in Figure 10a. Site A is over the center of the body, site B is on the body 25 m inward from the right edge, and sites C, D, and E are 25, 50, and 100 m away from the right edge of the body, respectively. The CSEM anomalies are presented in Figure 10b-d and show the response ratios of this model to the model without the near-surface resistor.

The impact of the near-surface feature is significant and varies with component. The maximum effect in all components occurs when the source is located over the resistive body, in agreement with a previous study of 3D Fréchet derivatives that illustrated a strong sensitivity to seawater and seafloor conductivity in the region immediately surrounding the transmitter (Weiss and Constable, 2006). When the source is away from the body, a 40–50% anomaly is observed in the vertical electric field (Figure 10c) for the two sites located over the body, sites A and B. Site C, the first site off of the body, exhibits an approximately 7% effect. The effect on the radial electric field (Figure 10b) is less and reaches a maximum of 8–12% for the sites that straddle the boundary of the near-surface body. The least effect (<5%) is for the azimuthal magnetic field (Figure 10d).

Note that the effect observed in Figure 10b and c extends over a broad range of transmitter-receiver separations and could confound an interpretation, especially if such shallow bodies were common within the survey area. This is a principal argument for precise placement of receivers for repeat reservoir monitoring measurements because imprecise receiver replacement near a feature like this could lead to false reservoir-depletion anomalies. This is also an important consideration in exploration surveys in areas where near-surface inhomogeneities such as hydrates are suspected. Although not shown here, we have modeled the analogous scenario where an isolated shallow body is below the transmitter and is located several kilometers from the receivers. As anticipated, the anomaly produced by this feature is confined to data collected only when the transmitter is located over the body.

### Effect of ocean conductivity

In Figure 11, we investigate the effect of seawater resistivity, which changes over time because of salinity and thermal variations associated with ocean currents and river outflows. We examine the variation in response when seawater resistivity changes from the 0.330-ohm-m value used in the previous models to a new value of 0.315 ohm-m (a 4.5% difference).

The results in Figure 11 show a variation in response of up to 10% in amplitude and a few degrees in phase. The strongest change is in the $E_y$ and $B_x$ components and occurs when the influence of the airwave is strongest, at transmitter-receiver offsets of 10 km and greater. This is explained because the airwave must travel through the entire water column and the attenuation of the signal within the seawater is strongly a function of conductivity. If time-lapse survey data were compared without accounting for a change in seawater resistivity, a false depletion anomaly might result.

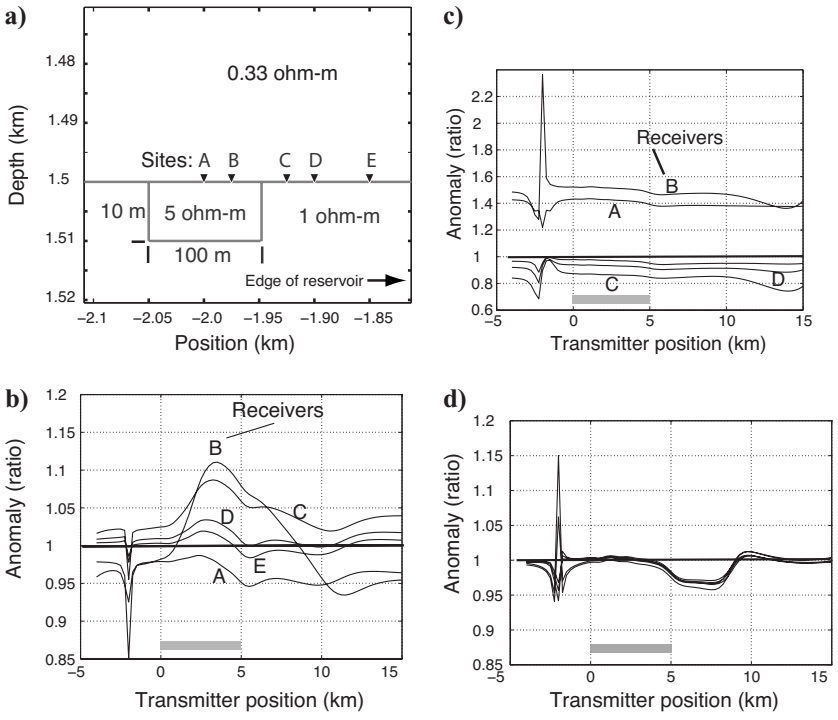


Figure 10. The effect of a seafloor inhomogeneity. Ratio of CSEM response of the 2D canonical model (without seafloor inhomogeneity) to that with the seafloor inhomogeneity. (a) Receiver locations, (b) inline electric field $E_y$, (c) vertical electric field $E_z$, and (d) azimuthal magnetic field $B_x$.

A precise analysis of CSEM results thus requires precise knowledge of the characteristics of the seawater. This should not be a problem because the commonly used conductivity-temperature-depth (CTD) probes accurately measure the seawater properties. However, interpretation and modeling for the level of accuracy required for time-lapse CSEM requires that these data be acquired at the time CSEM data are recorded. Because seawater temperature variations are strongest in the upper few hundred meters of the water column, this problem is most severe for shallow-water applications.

## Errors in transmitter geometry and receiver locations

Given adverse weather conditions and strong ocean currents, the transmitter antenna vector often can be rotated from ideal survey specifications. In Figure 12, we investigate the effects of transmitter dipole pitch variations of 10° up and down, where we plot the ratio of the response for the dipping dipole to a purely horizontal dipole. The false anomalies this produces vary spatially and are greatest when the transmitter is near the receivers. When the transmitter is more than a few kilometers away, both the 10° dip-down (Figure 12a) 10° dip-up (Figure 12b) transmitters result in a somewhat smaller variation in response of about 15–20%. For the case of a dipole yaw and the symmetric model considered here, the perturbation is described by a cosine (yaw angle) scaling. These effects must be taken into account, because they are equal to or greater than the effects observed from reservoir flooding. We have modeled a dipping point dipole, whereas dip in the finite-length bipoles used in field surveys results in one electrode being closer to the seafloor, so the effect of dip will probably be greater than is shown here.

Last, we investigate the effect of an error in the lateral location of the receiver (or transmitter). Figure 13 shows the response variation as we move the receiver 25 and 50 m from its correct position. Again, the false anomaly this produces is largest when the transmitter is over the receiver. When the transmitter is at least a few kilometers away, a 50-m lateral position error (Figure 13b) results in a false anomaly of about 5%; a 25-m position error (Figure 13a) yields a smaller, approximately 2% anomaly. These false anomalies extend well to the right of the reservoir boundary. Extrapolation of these results suggests that seafloor receiver positions should be known and repeatable to less than 5–10 m accuracy to detect time-lapse depletion anomalies.

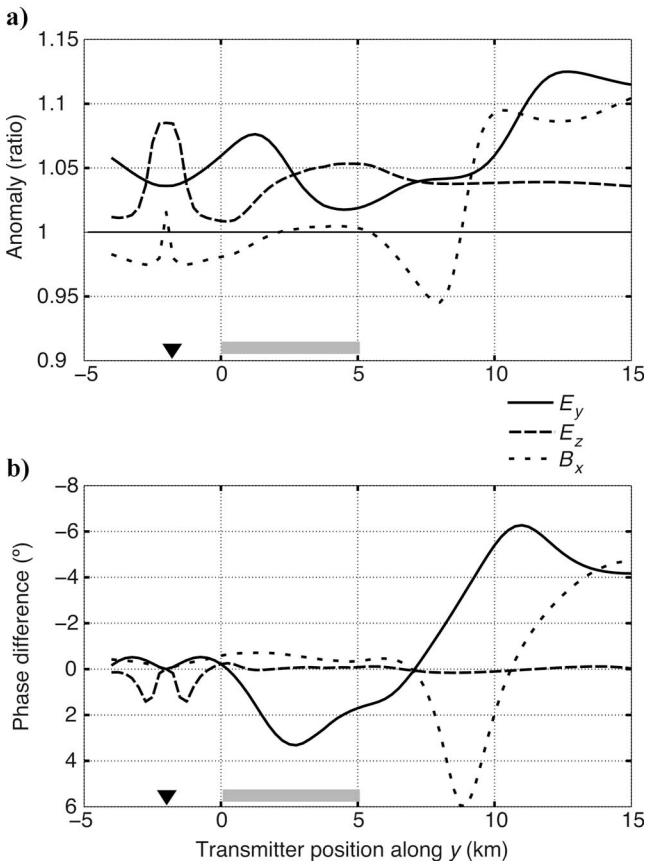


Figure 11. Effect of seawater conductivity variations on CSEM (a) anomaly ratio and (b) phase difference. Ratio of 2D canonical response with 0.33-ohm-m seawater to that with 0.315-ohm-m seawater (a 4.5% difference).

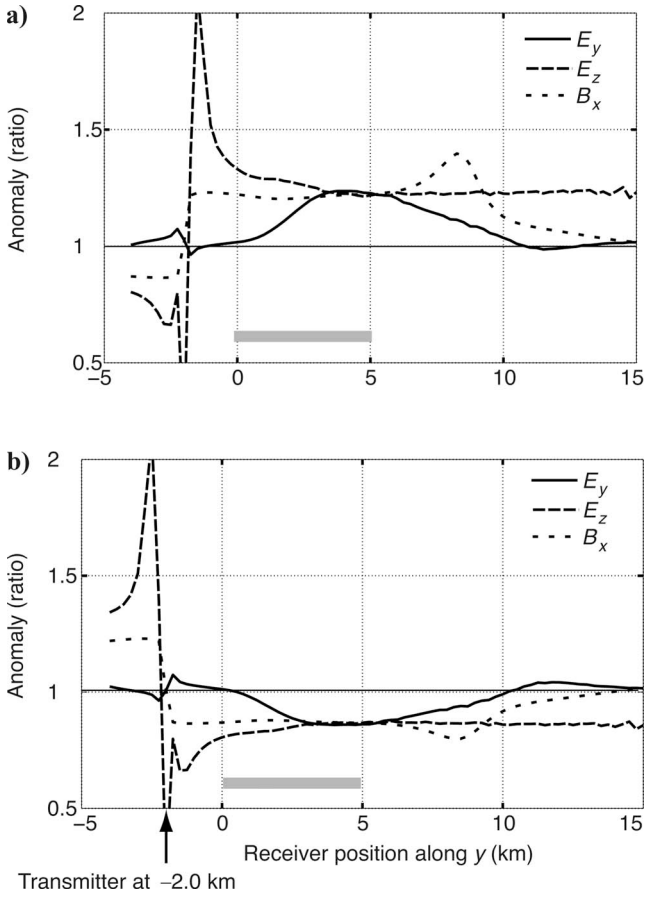


Figure 12. Effect of transmitter dipole dip. Ratio of 2D canonical response with transmitter dipole dipping to that with a horizontal dipole: (a) dip 10° down; (b) dip 10° up.

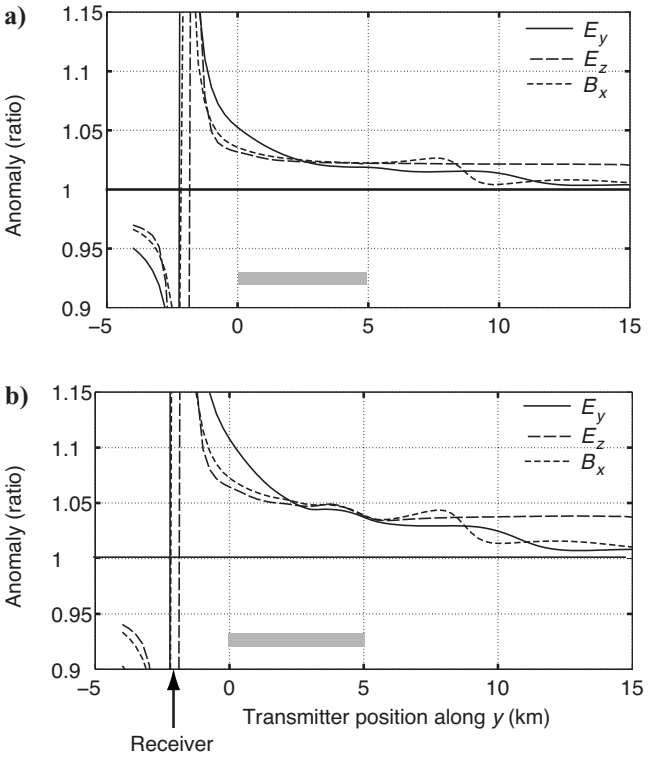


Figure 13. Effect of error in receiver location. Ratio of response with receiver at −2 km to response with receiver at (a) 25 m and (b) 50 m to the left.

## CONCLUSIONS

We have shown through a series of 2D model studies that a depleting reservoir can produce small but measureable changes in CSEM response over time, and these changes can be characteristic of the depletion geometry. It is understood that 3D analysis of more complex and realistic reservoir scenarios will be required to provide guidance for practical applications. However, our studies suggest that being able to provide useful information on reservoir geometry and resistivity to the reservoir engineer during production will require the ability to resolve changes in the CSEM response over time of at best a few percent. This in turn will require repeatability of the basic CSEM measurement to 1%–2% or better. This is probably not possible using the current technology of free-falling receivers, towed transmitters, and supershort baseline positioning technology, especially in deepwater areas.

There are several possible solutions, and the CSEM industry will be challenged to find those that provide the required accuracy yet remain cost effective. Obviously, permanent installation of EM receivers and transmitters on the seafloor would be an attractive alternative, but this is likely to be impractical. Permanent monuments to which receivers and transmitters could be affixed by remotely operated vehicles is an attractive approach because the position repeatability could be on the order of 1 m or less. This approach mitigates the effect of unknown seafloor inhomogeneities as well as the often large uncertainties in position, altitude, dip, and yaw of a deep-towed source antenna. Accurate characterization of the electrical properties of the water column is possible through the use of CTD instrumentation, routinely used by oceanographers worldwide.

Yet another factor to consider for the repeatability of CSEM measurements is changes to oilfield infrastructure — the pipelines, cables, steel templates, etc., installed on the seafloor during the life of a producing reservoir. Given their limited spatial extent, it may be possible to plan time-lapse measurements so that source-receiver paths largely avoid such structures, but certainly there will be survey geometries where crossing infrastructure is unavoidable. Steel casings and other conductive infrastructure have much smaller skin depths than seawater and sediments and may distort the CSEM transmissions locally. Such distortions are probably confined to where the transmitter or receivers are located close to infrastructure, but careful modeling and analysis will be required to demonstrate this point.

In summary, time-lapse CSEM is likely to be a most demanding application of EM geophysics, but there is nothing that we have examined so far that implies it is impossible.

## ACKNOWLEDGMENTS

This work was carried out under support from the Seafloor Electromagnetic Methods Consortium at Scripps Institution of Oceanography. Three reviewers provided helpful comments.

## REFERENCES

Constable, S., and L. J. Srnka, 2007, An introduction to marine controlled-source electromagnetic methods for hydrocarbon exploration: Geophysics **72**, no. 2, WA3–WA12.

Constable, S., and C. J. Weiss, 2006, Mapping thin resistors and hydrocarbons with marine EM methods: Insights from 1D modeling: Geophysics **71**, no. 2, G43–G51.

Darnet, M., M. C. K. Choo, R.-E. Plessix, M. L. Rosenquist, K. Yip-Cheong, E. Sims, and J. W. K. Voon, 2007, Detecting hydrocarbon reservoirs from CSEM data in complex settings: Application to deepwater Sabah, Malaysia: Geophysics **72**, no. 2, WA97–WA103.

Ellingsrud, S., T. Eidesmo, S. Johansen, M. Sinha, L. MacGregor, and S. Constable, 2002, Remote sensing of hydrocarbon layers by seabed logging (SBL): Results from a cruise offshore Angola: The Leading Edge, **21**, 972–982.

Hoversten, G. M., F. Cassassuce, E. Gasperikova, G. A. Newman, J. Chen, Y. Rubin, Z. Hou, and D. Vasco, 2006, Direct reservoir parameter estimation using joint inversion of marine seismic AVA and CSEM data: Geophysics, **71**, no. 3, C1–C13.

Landro, M., H. H. Veire, K. Duffaut, and N. Najjar, 2003, Discrimination between pressure and fluid saturation changes from marine multicomponent time-lapse seismic data: Geophysics, **68**, 1592–1599.

Li, Y., and K. Key, 2007, 2D marine controlled-source electromagnetic modeling: Part 1 — An adaptive finite element algorithm: Geophysics, **72**, no. 2, WA51–WA62.

Lien, M., and T. Mannseth, 2008, Sensitivity study of marine CSEM data for reservoir production monitoring: Geophysics, **73**, no. 4, F151–F163.

Vasco, D. W., H. Keers, J. Khazanehdari, and A. Cooke, 2008, Seismic imaging of reservoir flow properties: Resolving water influx and reservoir permeability: Geophysics, **73**, no. 1, O1–O13.

Wahrmund, L. A., K. E. Green, D. Pavlov, and B. A. Gregory, 2006, Rapid interpretation of CSEM reconnaissance data: 76th Annual International Meeting, SEG, Expanded Abstracts, 709–713.

Weidelt, P., 2007, Guided waves in marine CSEM: Geophysical Journal International, **171**, 153–176.

Weiss, C. J., and S. Constable, 2006, Mapping thin resistors in the marine environment, Part II: Modeling and analysis in 3D: Geophysics, **71**, no. 6, G321–G332.

Weitemeyer, K., S. Constable, K. Key, and J. Behrens, 2006, First results from a marine controlled-source electromagnetic survey to detect gas hydrates offshore Oregon: Geophysical Research Letters, **33**, L03304.